STRUCTURAL BIOLOGY

Cryo-EM structure of the mammalian ATP synthase tetramer bound with inhibitory protein IF1

Jinke Gu[1]*, Laixing Zhang[1]*, Shuai Zong[1]*, Runyu Guo[1]*, Tianya Liu[1], Jingbo Yi[1], Peiyi Wang[2], Wei Zhuo[1], Maojun Yang[1,3]†

The mitochondrial adenosine triphosphate (ATP) synthase produces most of the ATP required by mammalian cells. We isolated porcine tetrameric ATP synthase and solved its structure at 6.2-angstrom resolution using a single-particle cryo–electron microscopy method. Two classical V-shaped ATP synthase dimers lie antiparallel to each other to form an H-shaped ATP synthase tetramer, as viewed from the matrix. ATP synthase inhibitory factor subunit 1 (IF1) is a well-known in vivo inhibitor of mammalian ATP synthase at low pH. Two IF1 dimers link two ATP synthase dimers, which is consistent with the ATP synthase tetramer adopting an inhibited state. Within the tetramer, we refined structures of intact ATP synthase in two different rotational conformations at 3.34- and 3.45-Å resolution.

F_1F_O adenosine triphosphate (ATP) synthases are molecular motors that enable conversion of energy from a proton gradient to the high-energy terminal phosphodiester bond of ATP. The overall architecture of this multipart enzyme is largely conserved from bacteria to the mitochondria of eukaryotes (*1*–*3*). ATP synthases comprise the soluble F_1 hexagonal head plus central shaft and membrane-embedded F_O peripheral stalk and c-ring (*4*). The central shaft and c-ring form the well-known rotor, whereas the hexagonal head and peripheral stalk form the so-called stator. Because the number of protons required for one rotation, which generates three ATP molecules, is often not a multiple of three (*5*, *6*), it was proposed that torsion energy can be stored and released during the rotation cycle (*7*, *8*).

Oligomerization of ATP synthase is proposed to be involved in the formation of cristae in mitochondria (*9*, *10*). Two types of interfaces are proposed in oligomers: one between the two protomers in a dimer and another between dimers in row-like structures. A recent dimeric ATP synthase structure from yeast showed that subunit a and subunit i/j are major contributors for dimerization (*11*). It has been reported that the distance between protomers in a dimer of a given species is constant, but the distance between dimers within row-like structures is variable (*12*, *13*). This observation suggests that there are tight interactions within the dimer, but interactions between dimers are less constrained.

ATP synthase constitutes ~20% of the total membrane proteins present in mitochondria. Its ATP hydrolysis rate (>4000 molecules per second) is much higher than its ATP synthesis rate (~400 molecules per second), so it is critical to inhibit this enzyme when proton motive force across the inner membrane is lost (*14*). ATP synthase inhibitory factor subunit 1 (IF1) is an in vivo inhibitor of mammalian ATP synthase. As previously demonstrated (*15*, *16*), IF1 has two oligomeric states: dimer and tetramer. At pH 8.0, IF1 could form a tetramer through coiled-coil interactions involving the N-terminal inhibitory regions, thus preventing its inhibitory activity (*15*). However, when Δp level drops and pH plunges below 6.5 in matrix, IF1 disassembles into dimers, in which only the C-terminal regions form antiparallel coiled-coil interactions, and the N-terminal inhibitory regions are set free to insert into the F_1 heads (*17*).

In this study, we report a cryo–electron microscopy (cryo-EM) structure of a tetrameric ATP synthase from pig, *Sus scrofa domesticus*, bound with IF1 in a conformation that is consistent with an inhibited state. In our 6.2-Å tetrameric ATP synthase structure, we detected six sites of interactions between the two dimers. From this low-resolution complex, we extracted and solved substructures of two rotational states at 3.34 and 3.45 Å. The combination of low- and high-resolution information reveals mechanism for regulation of mammalian ATP synthase in which IF1 brings together dimers into a putatively non-productive tetramer.

Structure determination

In our previous studies (*18*), when we analyzed the cryo-EM data of the mitochondrial electron transfer chain supercomplexes and megacomplexes, we invariably found a minor population of particles that had an H-shaped architecture in the two-dimensional (2D) classification processes (fig. S1). Further analyses of these particles revealed that they belonged to a tetrameric ATP synthase complex, which is corresponding to the high-molecular-weight bands in previous biochemical clear-native polyacrylamide gel electrophoresis (CN-PAGE) analyses (*19*). We optimized protein purification procedures to obtain larger amounts of the tetrameric ATP synthase from fresh porcine hearts and collected cryo-EM images (fig. S2 and supplementary materials). We refined the structure of this tetrameric porcine ATP synthase to an overall resolution of 6.2 Å (Fig. 1, figs. S3 and S4, and table S1). Two V-shaped ATP synthase dimers are positioned nearly perpendicular to form an architecture with C2 symmetry. Structural comparison indicates that the two protomers within each dimer are in E-state and DP-state (Fig. 1).

In order to obtain high-resolution structures of subcomponents of the tetramer, we first reconstructed the density map of the tetrameric porcine ATP synthase at an overall resolution of 10.5 Å in C1 symmetry using a total of 179,323 twice-binned particle images (fig. S5A). The diagonal protomers adopt similar conformations. To obtain the overall F_1F_O density, we performed masked 3D classification focused on the F_1 section followed by classification of the selected particles with an F_1F_O mask. After 3D autorefining, we obtained both the E-state and the DP-state densities at overall 3.34- and 3.45-Å resolutions, respectively (figs. S5, B to D, and S6).

To obtain the local density of F_O section, the selected particles were first refined by using F_1F_O mask and then refined by using F_O mask. E-state and DP-state F_O section densities were determined at 3.94- and 4.35-Å resolutions overall, respectively (fig. S7). Using a combination of structure docking and de novo modeling, we built structural models of all 30 subunits in COOT (*20*); 26 subunits could be built with clear side chains (table S2). The side chains of subunits e, g, k, and 6.8PL (6.8 kDa proteolipid) are not well resolved (fig. S8 and table S2). The "gold standard" Fourier shell correlation criteria between the models and maps have no significant differences, indicating the absence of overfitting (figs. S9 and S10).

Overall structure of mammalian ATP synthase

The two ATP synthase states, E and DP, differ in the direction of the central shaft subunit γ, the conformation of subunits $\alpha_3\beta_3$, and the position of the peripheral stalk (Fig. 2), similar to previous reports (*21*, *22*). The subunit compositions are identical in both states, including all 18 previously identified ATP synthase subunits (*23*, *24*) and a newly detected subunit k. In 1994, Walker defined the α and β subunits in the $\alpha_3\beta_3$ head as α_E, β_E, α_{DP}, β_{DP}, α_{TP}, and β_{TP}, respectively, with nucleotide binding site in the β_E being empty, in the β_{DP} containing adenosine diphosphate (ADP), and in the β_{TP} containing adenylyl-imidodiphosphate

[1]Ministry of Education Key Laboratory of Protein Science, Tsinghua-Peking Joint Center for Life Sciences, Beijing Advanced Innovation Center for Structural Biology, School of Life Sciences, Tsinghua University, Beijing 100084, China. [2]SUSTech Cryo-EM Facility Center, Southern University of Science and Technology, Shenzhen 518055, China. [3]School of Pharmacy, Tongji Medical College, Huazhong University of Science and Technology, Wuhan 430030, China.
*These authors contributed equally to this work.
†Corresponding author. Email: maojunyang@tsinghua.edu.cn

(AMP-PNP). The α subunits all contain ATP (*17*, *25*, *26*) but are named according to the β subunit with which they form the intact catalytic site. Viewed from the N termini of the α and β subunits, β_{DP} is downstream of β_E, and β_{TP} is upstream of β_E, in a clockwise direction. In one state, the subunit α adjacent to the peripheral stalk is α_E, so we define this state as the E state for our structure. Likewise, in the other state, the subunit α adjacent to the peripheral stalk is α_{DP}, so we define this state as the DP state (Fig. 2) (*8*, *27*).

In this porcine ATP synthase structure, we identified a piece of density in the site occupied by subunit k in the yeast structure (Fig. 2 and figs. S8G and S11) (*11*, *27*). No subunit k is present in the bovine structure, and BLAST (Basic Local Alignment Search Tool) analysis indicated that no analog of yeast subunit k is present in mammalian ATP synthases. A recent report proposed that the human proteins DAPIT (diabetes-associated protein in insulin-sensitive tissue) and 6.8PL (6.8 kDa proteolipid) are analogs of subunits k and i/j in yeast, respectively (*23*). However, the density in our map corresponding to subunit i/j in the yeast structure is adequate to enable side chain building, and we assigned DAPIT to this density (fig. S8H). Besides, the N terminus of subunit b is assigned to a lateral helix over the membrane (Fig. 2), whereas this helix was assigned as subunit g in the yeast structure.

In addition to the density corresponding to yeast subunit k, we also identified a helical density in the center of the c_8-ring (fig. S12). Although we were unable to build the side chains of this subunit into the low-resolution density maps, we propose that this subunit may be the previously reported subunit 6.8PL for four reasons: (i) 6.8PL was found as a subunit of mammalian ATP synthase in previous biological and biochemical studies (*24*) and could not be assigned to the density corresponding to yeast subunit i/j because this density was built as subunit DAPIT in our structure. (ii) Secondary structure predictions clearly show that the N-terminal 45 amino acids of 6.8PL form a long helix, which is consistent with our density within the c_8-ring (fig. S12C). The density corresponding to subunit k contains a flexible N-terminal loop, suggesting that this density does not belong to 6.8PL (fig. S8G). (iii) The helix is close to the C terminus of subunit e (Fig. 2 and fig. S11), which is consistent with previous cross-linking studies (*28*). (iv) In a recent vacuolar H^+–adenosine triphosphatase (V-ATPase) structure (*29*), the elliptical c_{10}-ring is composed of eight c subunits, a subunit c′ and a subunit c″. Within the c_{10}-ring, two helical densities were identified and the authors assigned them to subunit Voa1 and the N terminus of subunit c″. Because our density map within the c_8-ring is not well resolved, we cannot exclude the possibility that this density belongs to a protein recruited into the c_8-ring when ATP synthase is inhibited. A structure with better defined density in this region will be needed to definitively establish the identity of this subunit.

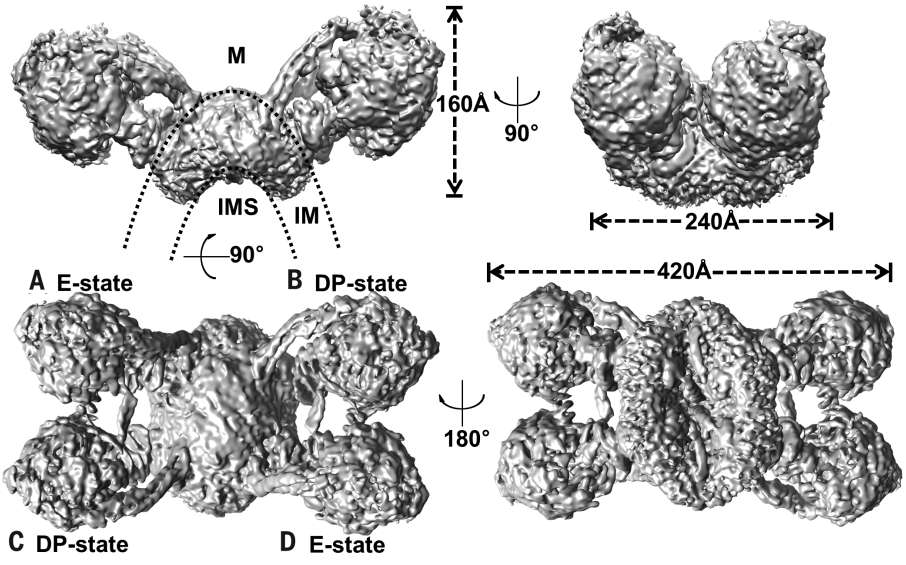

Fig. 1. Cryo-EM structure of a porcine ATP synthase tetramer. Cryo-EM map at 6.2-Å resolution displayed at 5σ contour level. M, matrix; IM, inner membrane; IMS, intermembrane space.

Conformational changes between two states of ATP synthase

Alignment of the E-state and DP-state models based on subunit a of the F_O section showed that the transmembrane helices of subunits b, e, f, g, k, A6L, and DAPIT match quite well between the two states (fig. S13, A and B), indicating that these helices are stably anchored in the membrane. Conversely, the c_8-ring and the peripheral stalk adopt different positions in the two states, indicating that these subunits move along with the rotation of the central shaft.

Alignment of the two states based on the F_1 section reveals that the conformation of the peripheral stalk and central shaft changes increasingly from top to bottom (fig. S13C). The $\alpha_3\beta_3$ heads, the top regions of the central shaft, and even the IF1 inhibitors are extremely well matched (fig. S13, C and D), suggesting that the conformation of the $\alpha_E\beta_E$ pair, $\alpha_{DP}\beta_{DP}$ pair, and $\alpha_{TP}\beta_{TP}$ pair is constant during each rotation step of the catalytic cycle. The lower part of the central shaft comprising subunits δ and ε is only slightly changed, whereas the c_8-ring is obviously rotated (fig. S13C).

Between the E and DP states, the central shafts have rotated by around 120°. We noticed that D194 in subunit γ can interact with R38 of one of the eight c subunits (fig. S14); thus, this R38 could potentially be used as a marker to distinguish a specific c subunit in the ring. Between the two states, the corresponding c subunit rotates ~140°, indicating that torsion must occur within the rotor during rotation. Considering that there are three αβ pairs but eight c subunits, the observed torsion is reasonable and consistent with previous reports (*21*, *30*, *31*). The conformations of the F_1 section and the c_8-ring are nearly unchanged on their own, so we conclude that torsion within the rotor between each catalytic step happens at the interaction surface between the central shaft and the c_8-ring. (Single-letter abbreviations for the amino acid residues are as follows: A, Ala; C, Cys; D, Asp; E, Glu; F, Phe; G, Gly; H, His; I, Ile; K, Lys; L, Leu; M, Met; N, Asn; P, Pro; Q, Gln; R, Arg; S, Ser; T, Thr; V, Val; W, Trp; and Y, Tyr.)

The linkage between the F_1 and F_O sections

Consistent with the previous structural findings (*8*, *11*, *21*, *22*, *27*, *32*), in our E- and DP-state porcine ATP synthase structures, the F_1 and F_O sections are linked at two sites. One is at the top of the overall structure between the N-terminal domain of the $\alpha_3\beta_3$ head and the hook of the peripheral stalk (fig. S14, A to C). This link is mediated by the conserved subunit OSCP (oligomycin sensitivity conferral protein), which has N- and C-terminal domains. The C-terminal domain is in contact with subunit F6 and bends the subunit b C-terminal helix into a hook (figs. S14, A and B, and S15A). In agreement with the chloroplast ATP synthase structure, the N-terminal helix of the α_E subunit can interact with subunit b, and the N-terminal helix of F6 and the C-terminal domain of OSCP hitch the $\alpha_3\beta_3$ head onto the hook of the peripheral stalk (*8*, *27*). The N-terminal domain of OSCP forms stable interactions with the N-terminal helix of α_{TP}, but the N-terminal helix of α_{DP} is ambiguous in our structure (fig. S14, A and C). However, the density map of the N-terminal helix of α_{DP} is blurred, probably because of disorder in this helix. Another linking site is at the membrane surface between the central shaft and the c_8-ring. In subunit c, the loop linking the N- and C-terminal helices is responsible for interacting with residues from subunit γ, δ, and ε. According to our density map, it is likely that all eight c subunits are involved in the

interaction with the central shaft (fig. S14, A and D). Comparing these linking sites between the E-state and DP-state structures indicates that although the stator has rotated around 120°, the interacting pattern between c_8-ring and the central shaft remains largely unchanged (figs. S13A and S14D).

The ADP-inhibited state F_1 section

The E-state and DP-state models mainly differ in the position of the peripheral stalk, the orientation of the central shaft, and the corresponding conformational change of $\alpha_3\beta_3$ heads (Fig. 2 and fig. S13). Because the subunit composition and interactions between subunits are similar within both states, we focused on the E-state F_1 section. The classic N-terminal β-barrels of α and β subunits alternate, forming a crown on top of the head (Fig. 3, A and B, and fig. S15B). Alignment of the three αβ pairs based on the α subunit reveals shifts in β_E and β_{TP} relative to β_{DP} (Fig. 3B). The nucleotide binding position of β_E is disrupted, and the C-terminal region of β_E is forced to acquire an "open" conformation. On the basis of comparison of the E-state F_1 section with the previous bovine structure (without the IF1 protein), we propose that this disorder may be caused by the orientation of subunit γ and insertion of IF1 (fig. S16) (*15*, *33*, *34*).

In the mammalian central shaft, only the N- and C-terminal long helices of γ subunit protrude into the center of the $\alpha_3\beta_3$ head (Fig. 3A), whereas δ and ε subunits bind to the root of γ subunit and interact with the membrane-embedded c_8-ring (fig. S14, A and D). The N-terminal helix of γ subunit reaches the C-terminal domain of the $\alpha_3\beta_3$ head, whereas the C-terminal helix of γ subunit can reach the top of the nucleotide binding region of the $\alpha_3\beta_3$ head (Fig. 3A). The convex side of the N-terminal helix of γ subunit points toward the α_E and β_E subunits, and the C-terminal helix of γ subunit primarily contacts loops from the α_{TP} and β_{TP} subunits (Fig. 3A) (*14*, *35*–*40*).

According to the "binding change mechanism," during either ATP synthesis or ATP hydrolysis, the relative position of β_E, β_{DP}, and β_{TP} is constant. β_E is in an open conformation, with the nucleotide binding site being empty waiting for accepting new ADP or ATP; β_{DP} is in a "loose" conformation bound with ADP and Pi, ready for synthesizing or ejecting; and β_{TP} is in a "tight" conformation bound with ATP, waiting to be released or hydrolyzed (*4*, *31*, *41*). However, structural data suggests that in some conditions, β_E subunits are not empty, and the nucleotides bound in the β_{DP} or β_{TP} subunits do not strictly correspond to the DP and TP names (*1*, *26*). Correspondingly, not all β_{DP} subunits occur in the loose state, and not all β_{TP} subunits are in the tight state. These discrepancies can be interpreted

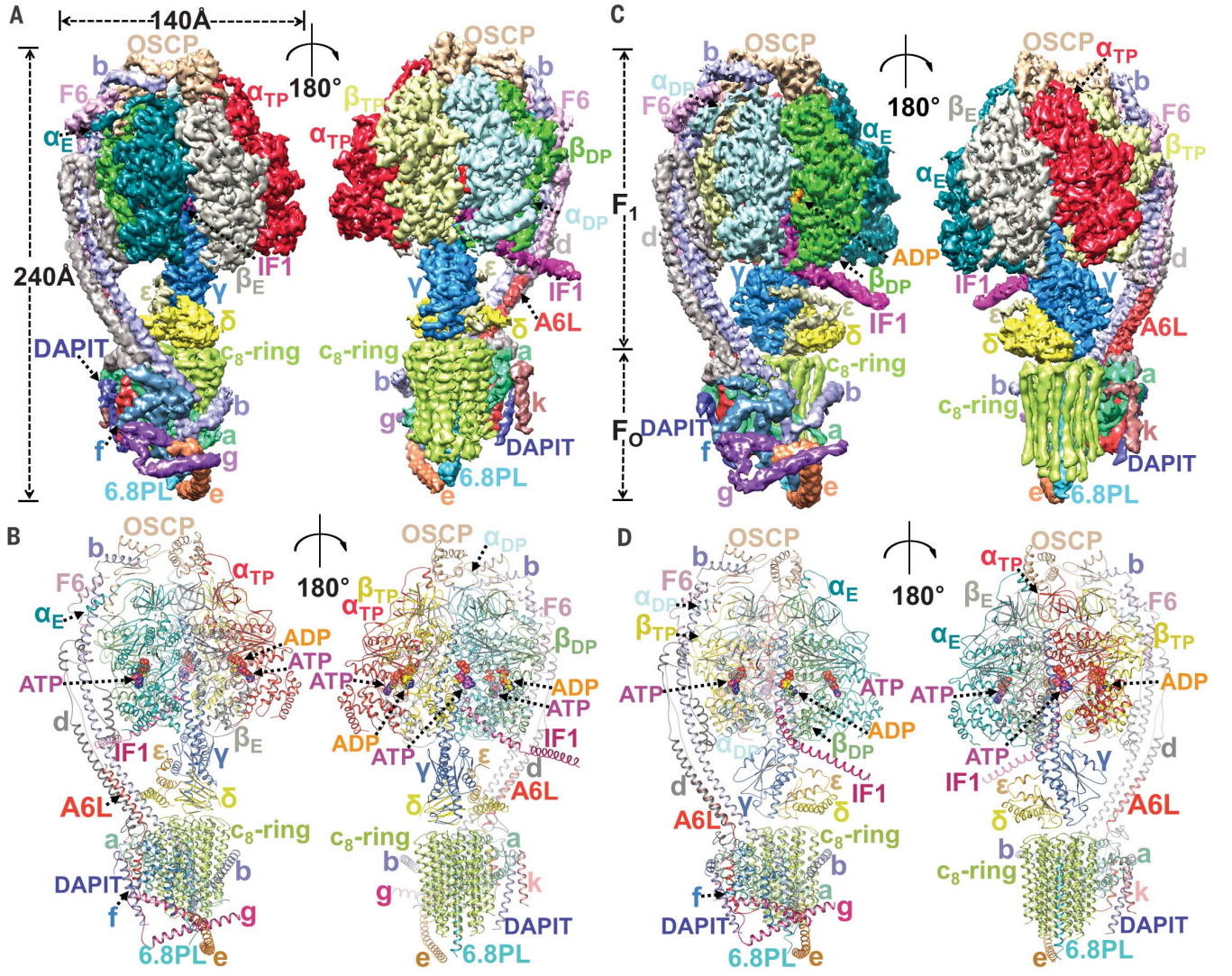

Fig. 2. Overall structures of E-state and DP-state ATP synthase. (**A** and **C**) Cryo-EM maps of (A) E-state ATP synthase at 3.45 Å (at 3σ contour level) and (C) DP-state ATP synthase at 3.34 Å (at 3σ contour level). (**B** and **D**) Cartoon representations of 3D reconstruction of substates extracted through focused alignment.

as relevant to the inhibited state or a catalytic intermediate. The only conclusion we can draw is that the structural differences between the β_{DP} and β_{TP} subunits are small. In our structure, all the α subunits are bound with MgATP, and all the nucleotide binding sites in the β_E subunits are empty. However, all the β_{DP} and β_{TP} subunits are tightly bound with MgADP without free Pi (Fig. 3, B to D). The β_{DP} and β_{TP} subunits in our structures may thus represent the non-competitive ADP-inhibited state (*14*).

The complete porcine F_O section

The F_O section is composed of a soluble matrix peripheral stalk and a membrane-embedded domain (Fig. 4A). The soluble portion of the subunit b C-terminal helix protrudes out from the membrane root and forms the backbone of the peripheral stalk (Fig. 4A). ATP synthases from chloroplasts and most bacteria contain two b subunits that protrude from the membrane: b and b′, with subunit b′ accompanying subunit b and inducing the latter to form a hook at the top region (*8*, *21*, *37*, *42*, *43*). By contrast, our work shows that the ATP synthase from porcine mitochondria only contains one b subunit, with the role of subunit b′ being replaced by subunit F6 at the top region, subunit d at the root region, and subunit A6L in the membrane (Fig. 4A) (*44*). Polar contacts between subunit F6 and subunit b bend the top region around 90° to form a hook (fig. S14, A and B). The C-terminal region of subunit d locks the root of subunit b, and two N-terminal helices of subunit d form a hairpin structure accompanying the middle region of subunit b to add extra plasticity and tenacity to this region (Fig. 4A and fig. S14A). The soluble portion of the subunit b C-terminal helix can obviously bend with its membrane portion, indicating that the peripheral stalk is capable of storing torsion energy. Consistent with previous studies (*28*, *30*), the C-terminal helix of the A6L subunit protrudes out from the membrane root and forms a three-helices bundle with subunits b and d, stabilizing the peripheral stalk (Fig. 4, A and B).

A total of 34 transmembrane helices can be detected within the membrane region (Fig. 4B and fig. S11), including a helix at the site of yeast subunit k and the helix inside the c_8-ring. We can clearly detect a piece of cylindrical density corresponding to a long α-helix containing more than 40 amino acids that extrudes from the top of the c_8-ring to the intermembrane space (IMS) (Fig. 4, A and B, and fig. S12), but we cannot determine whether this helix rotates with the c_8-ring or not. As stated above, we assigned subunit 6.8PL to this density.

A distinct feature of the F_O membrane domain is the five lateral helices (H2 to H6) of subunit a, which form a stable curved belt against the continuously rotating c_8-ring (Fig. 4, B and C). As in previous structures (*2*, *11*, *30*), the concave surface of H5 and H6 directly interacts with the c_8-ring. The tip of H5 and H6 is locked by the membrane portion of subunit b C-terminal helix. At the opposite side, the tip of H5 and H4 is locked by the k subunit (Fig. 4, A to C, and fig. S11). At the convex side of the belt, H3 and H4 are locked by subunit A6L and by the DAPIT subunit. The vertical H1 of subunit a is aligned with subunit A6L and subunit f (Fig. 4B and fig. S11). These vertical helices—including the membrane portion of the subunit b C-terminal helix, A6L, DAPIT, f, and k—are very likely to function as an anchor to stabilize the subunit a.

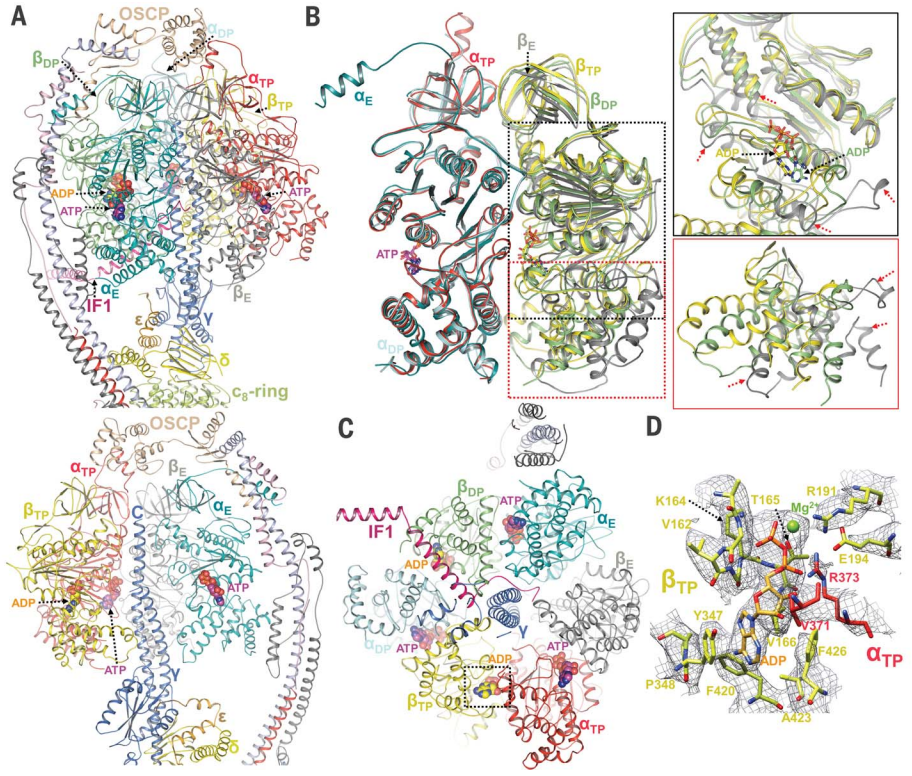

Fig. 3. The F_1 section of the IF1-bound E-state ATP synthase. (**A**) Side-on view of the F_1 section. The F_1 section structure was rotated 120° counterclockwise in the lower panel. (**B**) Alignment of the $\alpha_E\beta_E$, $\alpha_{TP}\beta_{TP}$, and $\alpha_{DP}\beta_{DP}$ pairs based on the α_{DP} subunit [root mean square deviation between the $\alpha_E\beta_E$ and $\alpha_{DP}\beta_{DP}$ pairs. ($RMSD_{E\ and\ DP}$) = 0.90 Å, RMSD between the $\alpha_{TP}\beta_{TP}$ and $\alpha_{DP}\beta_{DP}$ pairs. ($RMSD_{TP\ and\ DP}$) = 0.94 Å]. Black and red boxes indicate regions with major differences between the α/β pairs. (**C**) View of the IF1-inhibited F_1 head viewed from the IMS side. (**D**) The nucleotide binding site in the β_{TP} subunit is displayed at 4σ contour level.

Subunit e is a long, curved helix that crosses the membrane, subunit g comprises two helices that are embedded on the matrix side of the membrane, and the N-terminal helix of subunit b is positioned far away from the proton channel region (Fig. 4A and fig. S11). We propose that these helices can collectively account for the majority of the interactions occurring among the protomers in the tetramer. Given that subunit e and the C-terminal helix of subunit g are apparently tilted in the inner mitochondrial membrane, it is very likely that they are closely related to the bending known to occur for cristae.

The proton channels in the mammalian F_O section

Subunit c consists of two helices and adopts a hairpin shape. Eight c subunits form a circle, with the N-terminal helices arranged inward and the C-terminal helices arranged outward (Fig. 4B). The loops linking the N- and C-terminal helices interact with the central shaft of the F_1 section, including subunits γ, δ, and ε (fig. S14D). Surface electrostatic analysis showed that a circle of negative charges encircles the c_8-ring cylinder in the middle of the transmembrane helices (fig. S12D). These negative charges are mostly contributed by the conserved E58 residues of subunit c helices (Fig. 4D) because no charged residues exist in the vicinity of E58 in our porcine structure. According to previous structures of yeast and algal ATP synthase, these conserved E58 side chains could acquire two conformations (*27*, *45*, *46*). When protonated, these residues point inward to the c-ring in a "closed" conformation; when deprotonated, these residues point outward from the c-ring, acquiring an open conformation. It was previously proposed that only two E58 residues covered by subunit a are deprotonated in the open conformation, whereas the other six are protonated in the closed conformation, so when E58 encounters R159 in subunit a, the protons taken from E58 can be pumped across membrane (*46*). In our structure, all E58 residues are likely protonated in the closed conformation (Fig. 4, D and E) because no protons should translocate in the inhibited state.

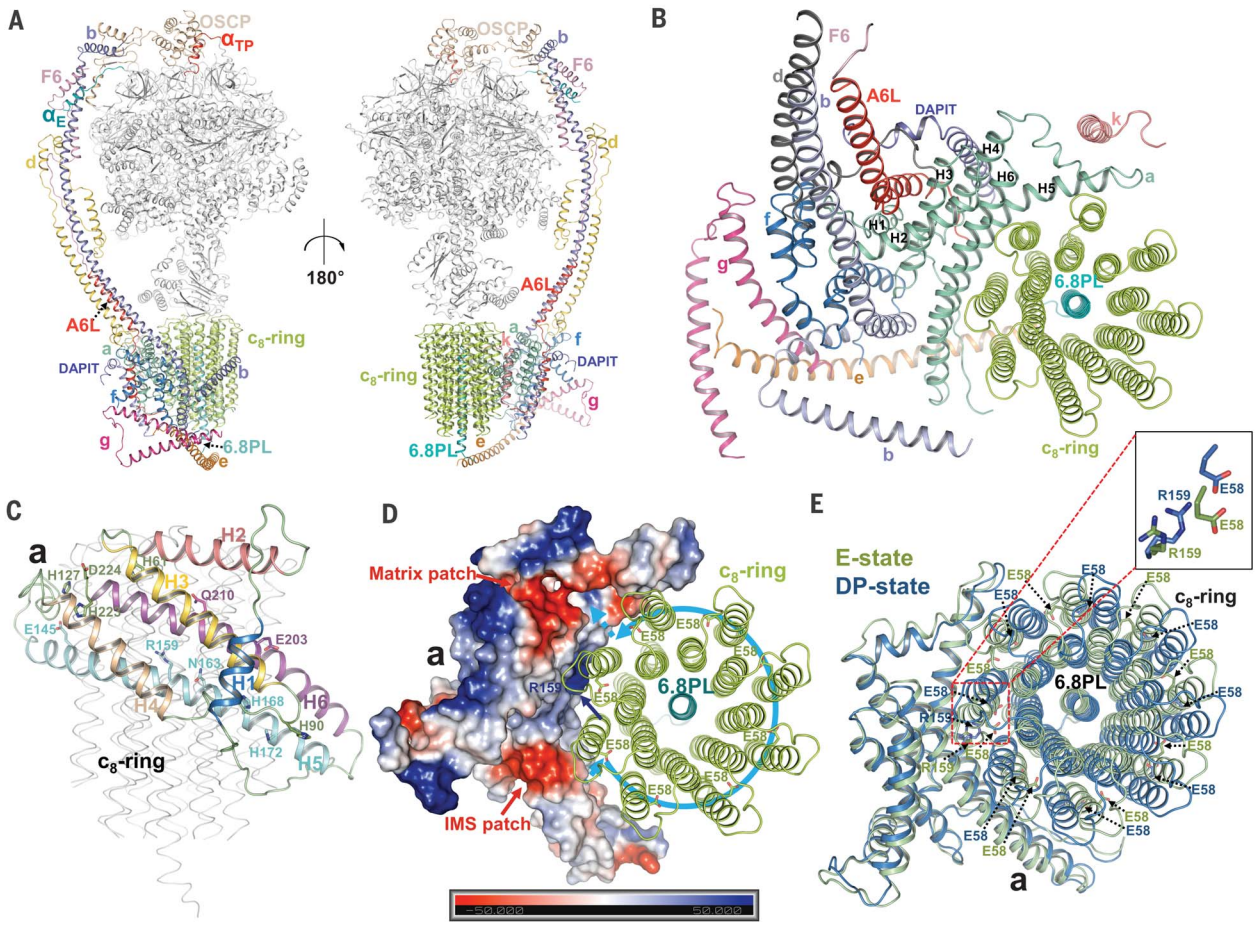

Fig. 4. The complete mammalian F_O section of ATP synthase. (**A**) Side views along the membrane highlighting the F_O section and OSCP. Other subunits are colored gray. (**B**) The F_O section membrane region viewed from the matrix side. (**C**) Subunit a residues forming the proton channel. (**D**) A charge-smoothed potential map of subunit a generated in PyMOL. (**E**) Comparison of subunit a and the c_8-ring of the E-state and DP-state. These two structures are aligned based on subunit a with a backbone root mean square deviation of 1.46 Å.

It was proposed that the two proton-pumping half channels of the F_O section are within the interface between subunit a and c_8-ring (*30*, *47*, *48*). In our structure, H5 and H6 of subunit a form a belt precisely holding the c_8-ring. Surface electrostatic analysis of subunit a showed three obviously charged patches on the belt (Fig. 4D). A positively charged subunit a residue R159 is located at the middle region of the belt, forming the central patch. Two negatively charged patches are separated at the two sides of the central patch. One negative patch is accessible to the matrix and forms an obvious half channel with the c_8-ring; we termed this the "matrix patch." The other negative patch is accessible to the IMS and forms a channel with subunit b on the opposite side of the c_8-ring, so we termed it the "IMS patch" (Fig. 4D). The negative charge of the matrix patch is mainly contributed by E145 and D224, and that of the IMS patch is mainly contributed by E203 (Fig. 4C). Compared with two recent yeast structures (*11*, *27*), the E203 side chain points to subunit b in our structure but points to subunit c in the yeast structures. When the side chain of E203 is pointing to subunit b, no proton can be transferred to E58 from the IMS, a situation that is consistent with the putatively IF1-inhibited state of ATP synthase tetrameric structure.

The relative position between subunit a and the c_8-ring is different in the two resolved states. When we aligned the two a subunits for the E-state and DP-state models, we observed a ~20° rotation in the position of the c_8-ring between the two states. In the E-state, the conserved E58 residue of subunit c is closest to the R159 residue of subunit a, even though its side chain is in the closed conformation. However, in the DP-state, clockwise rotation (viewed from the mitochondrial matrix) disrupts the interaction between E58 and R159, and R159 acquires a different orientation from that in the E-state (Fig. 4E), indicating that this DP-state structure may be in an intermediate c_8-ring rotation state.

Interactions within the ATP synthase tetramer

We docked the high-resolution models of the E-state and DP-state ATP synthase into the 6.2-Å map of the tetramer to obtain the complete tetrameric structure (fig. S17). The F_1 sections of adjacent protomers are linked with a long, bow-shaped, antiparallel IF1 homodimer (Fig. 5, A and B), which is consistent with a previous crystal structure of the IF1-inhibited F_1 head (*17*). The rotational axes between protomers in the dimeric subcomplex are ~97°, and the axis between protomers adjacent in the tetramer is ~47° (fig. S18). The four F_O sections form extensive contacts that stabilize the tetramer (Fig. 5 and fig. S19), and self-dimerization of the IF1 protein pulls the two dimers close together within the tetramer (Fig. 5B). In the IF1-mediated protomer pair, the C-terminal regions of α_E (DP state, Gln^{475}) and α_{DP} (E state, Ser^{470}) are close to each other; the closest distance is within 4 Å (Fig. 5B and fig. S17C). In the classic V-shaped dimer, the F_O membrane regions of the two protomers are loosely connected, and the F_1 sections are separated by a large gap (Fig. 5C and fig. S19).

We propose that the IF1-bound ATP synthase tetramer in our structure is an integral functional unit because the subunits in the protomers

interact with each other to stabilize the tetramer and regulate its function (Fig. 5 and fig. S19). The two dimers are linked to each other at six binding sites. For binding sites 1 and 6, two IF1 proteins form an antiparallel dimer that interacts with the F_1 heads within the mitochondrial matrix. Sites 2 to 4 are all above the membrane. Sites 2 and 4 include the N-terminal loop of subunit k and the N-terminal helix of subunit b from two adjacent dimers. Site 3 includes two N-terminal helices of g subunits from opposite protomers within the tetramer, positioned in parallel at the center of the structure (Fig. 6A). Site 5 is within the inner membrane, where two e subunits interact with each other (within the membrane), holding the tetramer together (Fig. 6B). Beyond these direct protein-protein interactions, the cryo-EM map clearly shows that there are additional densities in the membrane region, which we suspect may be filled by lipids.

In the middle region of the two protomers, the two curved domains formed by the e and g subunits with the N-terminal helix of subunit b are reminiscent of the previously reported BAR domain of the amphiphysin protein (Fig. 6 and fig. S19) (*11*, *49*); this BAR domain is able to bend the lipid bilayer through its amphipathic α helices. The two BAR-like domains in the center of our structure also form a dimer (Fig. 6). The membrane regions are likely bent by the perpendicular orientation of the ATP synthase dimers (fig. S18).

Discussion

Although ATP synthase structures from several species have been reported after the crystal structure of bovine F_1 subcomplex of ATP synthase (*26*), the complete mammalian ATP synthase structure has not been available. We obtained the tetrameric mammalian ATP synthase bound to IF1 and solved substructures in two different rotational states at overall resolutions of 3.34 and 3.45 Å. Among the 30 subunits in total (19 different types), b, k, DAPIT, and 6.8PL were differently assigned in our work as compared with previous reports (*11*, *23*, *30*). Alignment of the two rotational states showed that the central shaft has rotated around 120°, but the c_8-ring has rotated around 140°. We conclude from this result that torsional energy can be distributed over the central shaft and the peripheral stalk.

We identified two proton-pumping half channels that are accessible either to the IMS or to the matrix. Within the IMS half channel, a^{E203} points to subunit b in our structure rather than subunit c as in the yeast structure (fig. S20). The entire helix 6 of subunit a in our structure is shifted by one residue (one-third of a turn) compared with the yeast structure. This difference raises two possibilities. First, because we believe our ATP synthase may be in an inhibited state, the orientation of a^{E203} pointing to subunit b may be an inhibition mechanism to prevent proton transfer to subunit c. Second, we cannot exclude the possibility that conformational change of a^{E203} is required to pump protons in active state; in this condition, protons are absorbed into the membrane on one side of subunit a and expelled out of the membrane on the other side of subunit a. The conformational change of a^{E203} could transfer protons across subunit a. Further mutational studies of a^{E203} are needed to examine the function of this residue.

In the yeast dimer structure, the two protomers are linked by the long N-terminal loops of two a subunits that form an antiparallel β-sheet like a railing, and the long C-terminal loops of two i/j subunits contact each other. It was also proposed that the C-terminal regions of subunit k and subunit e can interact with each other in the IMS region (*11*). However, none of these interactions are evident in porcine ATP synthase. In mammals, the N-terminal sequence of subunit a is much shorter than in yeast (226 and 249 amino acids in pig and yeast, respectively), so the two a subunits in our structure do not form the railing that links the two protomers (figs. S19C and S21). Instead, the C-terminal loops of the

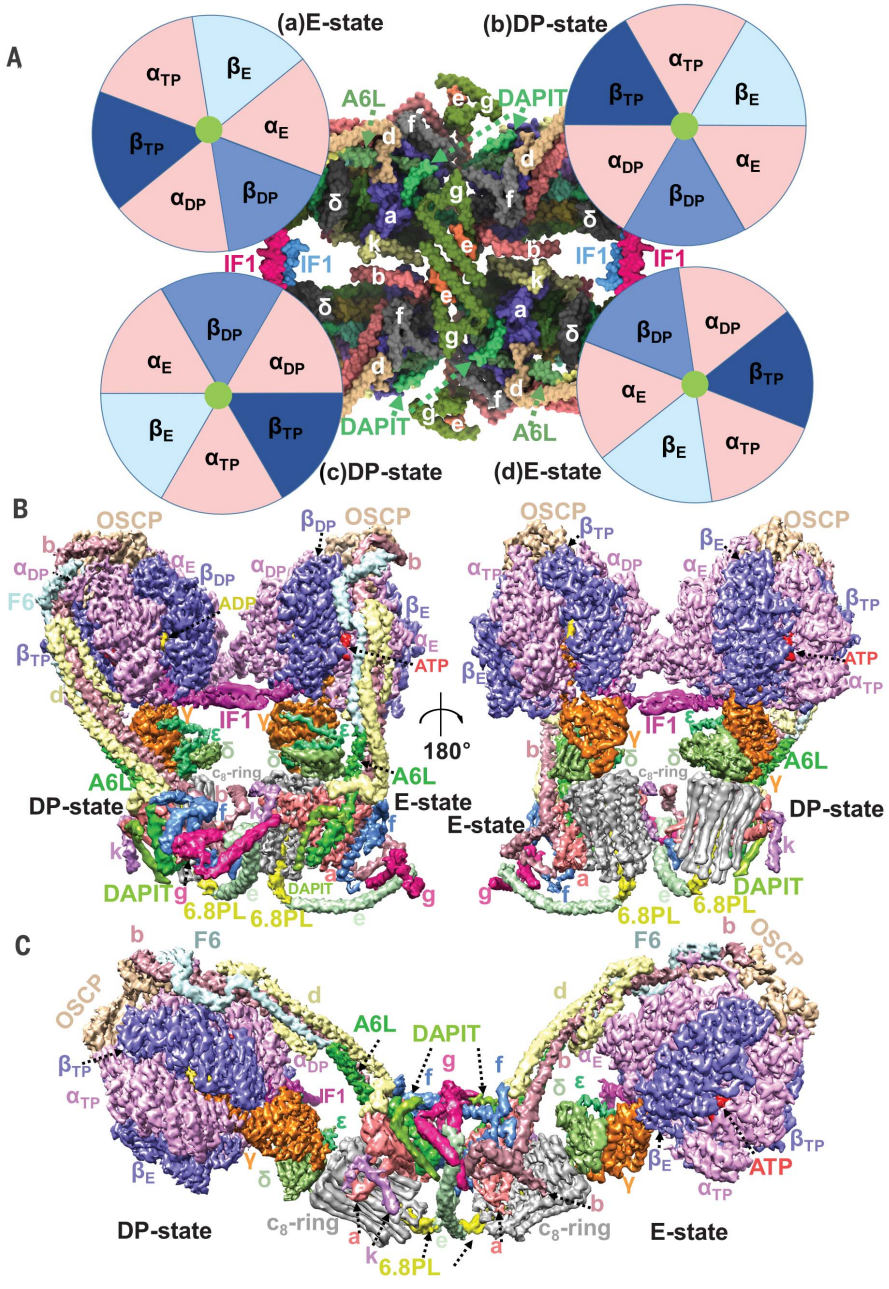

Fig. 5. Overall architecture of the porcine ATP synthase tetramer. (**A**) Schema of the porcine ATP synthase tetramer bound to IF1. (**B**) Cryo-EM map of the two IF1-linked ATP synthase protomers (at 3σ contour level). The maps of the extracted E-state and DP-state protomers were put together to generate the combined map. (**C**) Cryo-EM map of the V-shaped ATP synthase dimer (at 3σ contour level). The combined map was also generated by the extracted protomers.

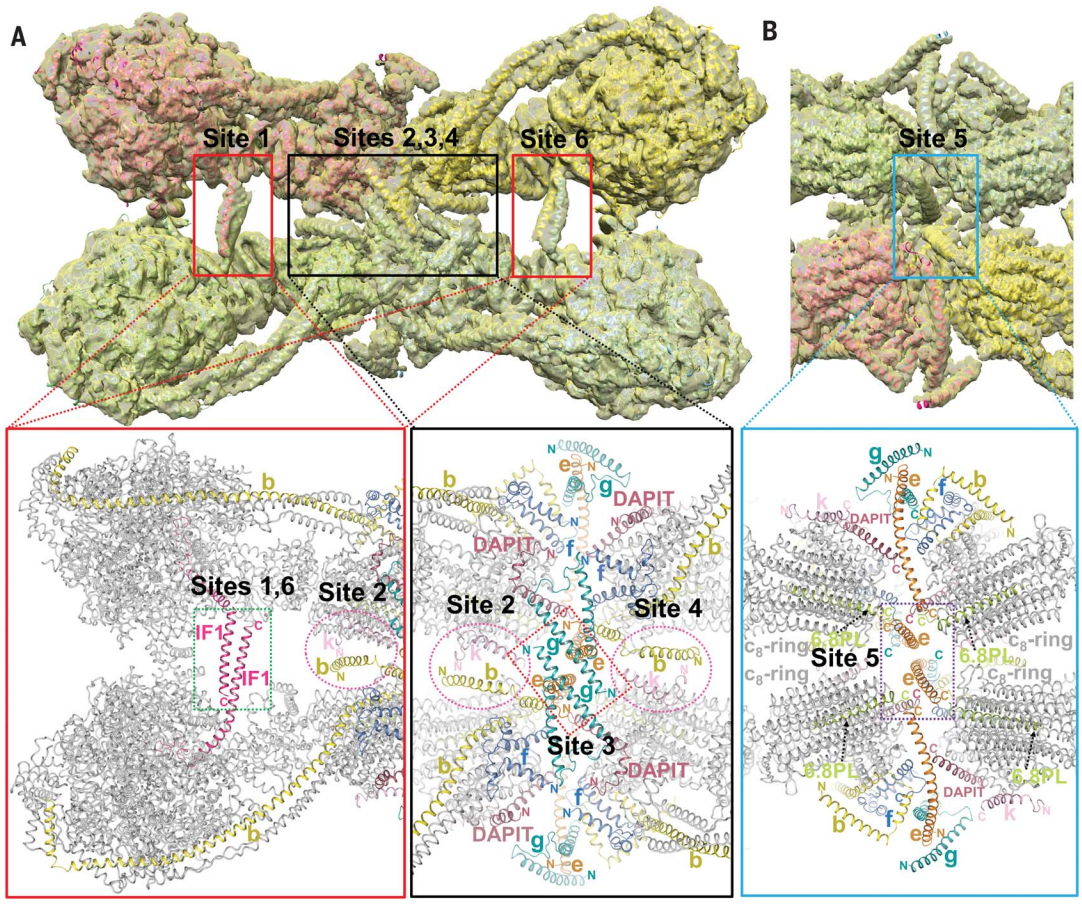

Fig. 6. The sites participating in the porcine ATP synthase tetramer formation. (**A**) Tetramer interaction sites viewed from the matrix side. High-resolution models were fit into the tetramer maps with a correlation coefficient of 0.85. (**B**) View from the IMS side.

DAPIT subunit and subunit f from the opposite protomer can form interactions. Presumably, the N-terminal helix of subunit k and the loop region of subunit g from the opposite protomer tend to form interactions (fig. S19C). On the basis of the increased variability in the angle between protomers in our porcine structure as opposed to the rigid structure in yeast (*11*), the interaction between two protomers may be weaker in mammals. Future functional studies are needed to show the relationship between the catalytic state of ATP synthase and the angle formed by the ATP synthase dimer.

Our structure suggests that ATP synthase tetramers can probably be inhibited by at least three mechanisms. The first mechanism is inhibition by IF1 protein dimers (fig. S22A). The long, stick-shaped IF1 dimer links the F_1 heads of protomers within different dimers, with its N-terminal regions inserted into the two $\alpha_{DP}\beta_{DP}$ pairs and contacting the two central γ subunits (fig. S22A). The second one is inhibition of the F_1 head by tightly bound MgADP (fig. S22B). As stated above, all the β_{DP} and β_{TP} subunits in the tetramer are tightly bound with an MgADP without free Pi, so these are in the widely recognized noncompetitive ADP-inhibited state (*14*). The third mechanism is inhibition by the long α-helical e subunits (fig. S22C). The C termini of the four e subunits are bent toward the four c_8-rings in each protomer, which—according to our unsharpened cryo-EM map—are able to interact with the C-terminal ends of the 6.8PL helices that fill the central hole inside the c_8-rings (fig. S23). We propose that these interactions may function as brake pads to block rotation of the c_8-rings in the inhibited state. Further studies are needed to confirm the identity of the protein within the c_8-ring. Whether it is 6.8PL or not, this protein could be involved in the regulation of ATP synthase activity.

Comparing the cryo-EM density maps of ATP synthase dimers from yeast and our structure (fig. S23), it is apparent that the C-termini of subunit e adopt different conformations. These helices of subunit e are straight in the yeast dimeric ATP synthase structure but are severely bent in our porcine tetramer structure (fig. S23D). The oligomerization of ATP synthase, and thus regulation of activity, should be intertwined with conformational changes in subunit e. Our assignment of the other interface subunits reveals intricate interactions in the tetrameric complex, supporting a functional role of this assembly in ATP synthase inhibition and suggesting roles for many supernumerary subunits with previously unknown or uncertain functions.

REFERENCES AND NOTES

1. W. Junge, N. Nelson, *Annu. Rev. Biochem.* **84**, 631–657 (2015).
2. H. Guo, J. L. Rubinstein, *Curr. Opin. Struct. Biol.* **52**, 71–79 (2018).
3. S. Cogliati, J. A. Enriquez, L. Scorrano, *Trends Biochem. Sci.* **41**, 261–273 (2016).
4. P. D. Boyer, *Annu. Rev. Biochem.* **66**, 717–749 (1997).
5. W. Kühlbrandt, K. M. Davies, *Trends Biochem. Sci.* **41**, 106–116 (2016).
6. K. M. Davies *et al.*, *J. Vis. Exp.* **91**, 51228 (2014).
7. H. Sielaff *et al.*, *Proc. Natl. Acad. Sci. U.S.A.* **105**, 17760–17765 (2008).
8. A. Hahn, J. Vonck, D. J. Mills, T. Meier, W. Kühlbrandt, *Science* **360**, eaat4318 (2018).
9. P. Paumard *et al.*, *EMBO J.* **21**, 221–230 (2002).
10. T. B. Blum, A. Hahn, T. Meier, K. M. Davies, W. Kühlbrandt, *Proc. Natl. Acad. Sci. U.S.A.* **116**, 4250–4255 (2019).
11. H. Guo, S. A. Bueler, J. L. Rubinstein, *Science* **358**, 936–940 (2017).
12. K. M. Davies, C. Anselmi, I. Wittig, J. D. Faraldo-Gómez, W. Kühlbrandt, *Proc. Natl. Acad. Sci. U.S.A.* **109**, 13602–13607 (2012).
13. K. M. Davies *et al.*, *Proc. Natl. Acad. Sci. U.S.A.* **108**, 14121–14126 (2011).
14. A. S. Lapashina, B. A. Feniouk, *Biochemistry* **83**, 1141–1160 (2018).
15. E. Cabezon, P. J. Butler, M. J. Runswick, J. E. Walker, *J. Biol. Chem.* **275**, 25460–25464 (2000).
16. E. Cabezón, M. J. Runswick, A. G. Leslie, J. E. Walker, *EMBO J.* **20**, 6990–6996 (2001).
17. E. Cabezón, M. G. Montgomery, A. G. Leslie, J. E. Walker, *Nat. Struct. Biol.* **10**, 744–750 (2003).
18. R. Guo, S. Zong, M. Wu, J. Gu, M. Yang, *Cell* **170**, 1247–1257. e12 (2017).
19. I. Wittig, H. Schägger, *Proteomics* **5**, 4338–4346 (2005).
20. P. Emsley, K. Cowtan, *Acta Crystallogr. D Biol. Crystallogr.* **60**, 2126–2132 (2004).
21. M. Sobti *et al.*, *eLife* **5**, e21598 (2016).
22. A. Zhou *et al.*, *eLife* **4**, e10180 (2015).

23. J. He *et al*., *Proc. Natl. Acad. Sci. U.S.A.* **115**, 2988–2993 (2018).
24. R. Chen, M. J. Runswick, J. Carroll, I. M. Fearnley, J. E. Walker, *FEBS Lett.* **581**, 3145–3148 (2007).
25. D. Stock, A. G. Leslie, J. E. Walker, *Science* **286**, 1700–1705 (1999).
26. J. P. Abrahams, A. G. Leslie, R. Lutter, J. E. Walker, *Nature* **370**, 621–628 (1994).
27. A. P. Srivastava *et al*., *Science* **360**, eaas9699 (2018).
28. J. Lee *et al*., *J. Biol. Chem.* **290**, 13308–13320 (2015).
29. S. H. Roh *et al*., *Mol. Cell* **69**, 993–1004.e3 (2018).
30. A. Hahn *et al*., *Mol. Cell* **63**, 445–456 (2016).
31. J. V. Bason, M. G. Montgomery, A. G. Leslie, J. E. Walker, *Proc. Natl. Acad. Sci. U.S.A.* **112**, 6009–6014 (2015).
32. A. W. Mühleip *et al*., *Proc. Natl. Acad. Sci. U.S.A.* **113**, 8442–8447 (2016).
33. M. Campanella, N. Parker, C. H. Tan, A. M. Hall, M. R. Duchen, *Trends Biochem. Sci.* **34**, 343–350 (2009).
34. M. E. Pullman, G. C. Monroy, *J. Biol. Chem.* **238**, 3762–3769 (1963).
35. L. R. Carrillo, J. E. Froehlich, J. A. Cruz, L. J. Savage, D. M. Kramer, *Plant J.* **87**, 654–663 (2016).
36. A. T. Jagendorf, *Photosynth. Res.* **73**, 233–241 (2002).
37. H. Sielaff, T. M. Duncan, M. Börsch, *Biochim. Biophys. Acta Bioenerg.* **1859**, 775–788 (2018).
38. C. M. Nalin, R. E. McCarty, *J. Biol. Chem.* **259**, 7275–7280 (1984).
39. M. Sekiya, R. K. Nakamoto, M. K. Al-Shawi, M. Nakanishi-Matsui, M. Futai, *J. Biol. Chem.* **284**, 22401–22410 (2009).
40. K. Y. Hara, Y. Kato-Yamada, Y. Kikuchi, T. Hisabori, M. Yoshida, *J. Biol. Chem.* **276**, 23969–23973 (2001).
41. W. Junge, H. Lill, S. Engelbrecht, *Trends Biochem. Sci.* **22**, 420–423 (1997).
42. J. E. Walker, *Biochem. Soc. Trans.* **41**, 1–16 (2013).
43. A. G. Stewart, L. K. Lee, M. Donohoe, J. J. Chaston, D. Stock, *Nat. Commun.* **3**, 687 (2012).
44. A. Dautant *et al*., *Front. Physiol.* **9**, 329 (2018).
45. J. Symersky *et al*., *Nat. Struct. Mol. Biol.* **19**, 485–491, S1 (2012).
46. D. Pogoryelov, O. Yildiz, J. D. Faraldo-Gómez, T. Meier, *Nat. Struct. Mol. Biol.* **16**, 1068–1073 (2009).
47. K. R. Vinothkumar, M. G. Montgomery, S. Liu, J. E. Walker, *Proc. Natl. Acad. Sci. U.S.A.* **113**, 12709–12714 (2016).
48. S. B. Vik, B. J. Antonio, *J. Biol. Chem.* **269**, 30364–30369 (1994).
49. B. J. Peter *et al*., *Science* **303**, 495–499 (2004).

ACKNOWLEDGMENTS

We thank the Cryo-EM Facility Center of Southern University of Science and Technology (Shenzhen) for providing the facility support. The computation was completed on the Yanglab GPU workstation. **Funding:** This work was supported by funds from the National Key R&D Program of China (2017YFA0504600 and 2016YFA0501100), the National Science Fund for Distinguished Young Scholars (31625008), the National Natural Science Foundation of China (21532004, 31570733 and 31800620), and the China Postdoctoral Science Foundation (2017M620040 and 2018T110091). **Author contributions:** M.Y. conceived, designed, and supervised the project; built the model; analyzed the data; and wrote the manuscript. J.G., T.L., J.Y., W.Z., and R.G. did the protein purification and detergent screening; J.G., P.W., and L.Z. performed EM sample preparation and data collection; J.G., L.Z., and S.Z. determined the structures. All authors discussed the manuscript data. **Competing interests:** The authors declare no competing interests. **Data and materials availability:** The atomic coordinates of the E-state F_O section, E-state, DP-state F_O section, DP-state, and tetramer of porcine ATP synthases have been deposited in the Worldwide Protein Data Bank with the accession codes 6J54, 6J5J, 6J5A, 6J5I, and 6J5K, respectively. The corresponding maps have been deposited in the Electron Microscopy Data Bank with the accession codes EMD-0668, EMD-0669, EMD-0670, EMD-0677, and EMD-0667.

SUPPLEMENTARY MATERIALS

science.sciencemag.org/content/364/6445/1068/suppl/DC1
Materials and Methods
Figs. S1 to S23
Table S1 and S2
References (*50*–*67*)

25 December 2018; accepted 23 May 2019
10.1126/science.aaw4852

Cryo-EM structure of the mammalian ATP synthase tetramer bound with inhibitory protein IF1

Jinke Gu, Laixing Zhang, Shuai Zong, Runyu Guo, Tianya Liu, Jingbo Yi, Peiyi Wang, Wei Zhuo and Maojun Yang

Science **364** (6445), 1068-1075.
DOI: 10.1126/science.aaw4852

ATP production under lockdown

Cellular processes must respond to change, often by speeding up, slowing down, or stopping altogether. Adenosine triphosphate (ATP) synthases use a transmembrane proton gradient to produce ATP, but this reaction can go in reverse and needs to be halted when conditions are unfavorable. Jinke Gu *et al.* purified a tetrameric ATP synthase complex from pig hearts that contained the endogenous inhibitory protein IF1. Targeted refinement yielded high-resolution views of the mammalian ATP synthase trapped in two different rotation states by IF1. The findings suggest that ATP synthase tetramers can be inhibited by at least three different mechanisms.

Science, this issue p. 1068